

Radio-millimetre investigation of galactic infrared dark clouds

D. Teyssier, P. Hennebelle and M. Pérault

Laboratoire de radioastronomie millimétrique, URA 336 du CNRS, École normale supérieure and Observatoire de Paris, 24 rue Lhomond, 75231 Paris cedex 05, France

Received 29 December 2000 / Accepted 13 November 2001

Abstract. We present follow-up observations of the mid-Infrared dark clouds selected from the ISOGAL inner Galaxy sample. On-the-fly maps of ^{13}CO , C^{18}O and the 1.2 mm continuum emission were conducted at the IRAM 30-m telescope, showing spectacular correlation with the mid-IR absorption. The dark clouds are distributed as far as the prominent molecular ring at a distance of 3 to 7 kpc from the Sun. The clouds exhibit shapes ranging from globules to thin filaments down to $\lesssim 1$ pc in size. The on-the-fly images obtained in ^{13}CO and C^{18}O confirmed that the cores are dense, compact molecular emitters, significantly more massive than local dark clouds (more than $1000 M_{\odot}$) and lie within low activity Giant Molecular Clouds (GMC's). Ratios of the emission in the $J = (2 - 1)$ and $(1 - 0)$ transitions of ^{13}CO and C^{18}O show a remarkable uniformity within each cloud, with a significant portion of the sample represented well by a ratio of 0.67 ± 0.12 . Preliminary analysis of temperature and density measurements reveals that most of the cores have densities above 10^5 cm^{-3} and temperatures between 8 and 25 K, these latter clouds being associated with young embedded stars. Despite the high extinction inferred from mid-IR ($A_V > 50$, Hennebelle et al. 2001), the molecular lines are surprisingly weak, indicating likely depletion onto cold grains.

Key words. ISM: clouds – molecules – structure – Radio continuum: ISM – Radio lines: ISM

1. Introduction

Galactic dark clouds observed in the mid-Infrared were first surveyed by ISO (Pérault et al. 1996), and turn out to be the highly condensed parts of Giant Molecular Clouds (GMC's) kiloparsecs away from the Sun. The ISOGAL survey imaged $\sim 10\%$ of the inner Galactic ridge, mostly towards relatively quiescent areas, in broad filters around 7 and $15 \mu\text{m}$ (Omont et al. 1999). A systematic analysis of the ISOGAL plates (Hennebelle et al. 2001, hereafter Paper I) allowed extraction of a catalogue of about 450 objects, most of them located in the inner Galaxy. The features are associated with GMC's lying between 3 and 7 kpc from us. In Paper I, we derived opacities at $15 \mu\text{m}$ in the range 1 to 4 for a few selected objects, leading to column densities of the order of 10^{23} cm^{-2} .

Similar findings have been reported by Egan et al. (1998) from the MSX (Midcourse Space Experiment) survey of the whole Galactic plane. They counted about 2000 IR dark clouds (IRDC's) located in the same distance range as the ISOGAL clouds and estimated extinctions at $8 \mu\text{m}$ in excess of 2. Detections of few clouds at millimetre wavelengths (Carey et al. 1998) confirmed that these objects are dense ($n_{\text{H}_2} > 10^5 \text{ cm}^{-3}$) and cold (T

$< 20 \text{ K}$). The authors conclude that these clouds are pre-protostellar cores where no sign of star-formation has been detected so far. This analysis was recently refined using continuum detection at 850 and $450 \mu\text{m}$ (Carey et al. 2000). The relatively high masses inferred from the sub-millimetre observations suggest a significant potential for stellar formation in these cores.

In the present paper we analyse spectroscopic and continuum follow-up observations of the ISOGAL dark features, conducted at the IRAM 30-m telescope. A sample of 13 objects has been mapped in several molecular tracers. A few characteristic physical parameters are inferred. The spatial resolution of these observations ($11''$ at 1.3 mm) opens the way to the analysis of the gas associated with the dense dust revealed by the mid-IR absorption at an intermediate spatial scale. Our main purpose is to compare the properties of our objects to those of the well-known local dark clouds. A subsequent study will provide an extensive analysis of temperature and density measurements and better assess the physico-chemical processes at work in the clouds (Teyssier et al. 2001b).

Sect. 2 presents the observational conditions and strategy. In Sect. 3 we describe the correlation between the millimetre emission and the IR absorption data. The nature of the different objects is assessed and a detailed spatial and spectral analysis is introduced. Sect. 4 gives the

Table 1. Line parameters

Species	Transitions	ν_0 (GHz)	HPBW ($''$)	T_{sys} (K)
^{13}CO	1 \rightarrow 0	110.201353	22.5	150-250
	2 \rightarrow 1	220.398686	11.2	400-900
C^{18}O	1 \rightarrow 0	109.782160	22.5	150-250
	2 \rightarrow 1	219.560319	11.3	400-900
HC_3N	9 \rightarrow 8	81.881468	30.2	130-250
	10 \rightarrow 9	90.978993	27.2	130-250
	11 \rightarrow 10	100.076389	24.7	130-250
CH_3CCH	5 ₀ \rightarrow 4 ₀	85.457300	28.9	130-250
	6 ₀ \rightarrow 5 ₀	102.547984	24.1	130-250
HCO^+	1 \rightarrow 0	89.188518	27.7	150-250
HCN	1 \rightarrow 0	88.631847	27.9	150-250

Note. – ν_0 is the rest frequency of the line, HPBW is the ideal half power beam width given by $1.2 \lambda/D$ where D is the telescope diameter and λ the line wavelength, T_{sys} is the SSB system temperature

physical properties of the clouds and their relation to the mid-IR opacities estimated in Paper I. Sect. 5 summarises our conclusions.

2. Observations

Observations of 13 IR dark clouds were conducted at the IRAM 30-m telescope between July 1998 and August 1999. Two summer runs were dedicated to spectroscopic observations, while continuum mapping at 1.2 mm was performed during winter time. Line and source parameters are listed in Tables 1 and 2.

2.1. Spectroscopic observations

Spectroscopic observations were performed during summertime under good to average weather conditions, in single-side band (SSB) mode, with receiver temperatures of about 90 K at 3 mm and 180 K at 1.3 mm. The data were calibrated to the T_{A}^* scale using the chopper wheel method (Penzias & Burrus, 1973). Discussion on the final brightness temperature scale T'_{mb} adopted for our data is presented in appendix A.1. Using comparison with observations of line calibrators (Mauersberger et al. 1989), we believe our absolute calibration to be better than 20%. The pointing accuracy was checked by repeated continuum scans across planets and strong quasars. The spectrometer was an autocorrelator set to a resolution of 80 kHz, yielding velocity channels of 0.24 km s^{-1} (0.1 km s^{-1}) at 3 mm (1.3 mm). Additional details on the technique used to correct for baseline spurious effects in the autocorrelator are given in appendix A.2

The maps were obtained with the Spectral Line On-the-Fly technique (Ungerechts et al. 1999) with a scanning speed of $1''/\text{second}$ (samples every 2 seconds) and a cross-scan sampling of $6''$. We used two classes of reference positions. The targets were mapped using a close-by reference position that was then compared to a further one chosen

Table 2. Source parameters

Name	RA (J2000.0)	Dec (J2000.0)	d ^(C) (kpc)
DF+04.36–0.06	17:55:53.07	-25:13:18.7	3.5
DF+09.86–0.04 ^(A)	18:07:37.22	-20:25:54.5	2.8
DF+15.05+0.09 ^(A)	18:17:37.87	-15:48:59.9	3.1
DF+18.56–0.15	18:25:19.52	-12:49:57.0	4.0
DF+18.79–0.03	18:25:19.84	-12:34:23.1	3.6
DF+25.90–0.17	18:39:10.13	-06:19:58.8	5.5
DF+30.23–0.20 ^(B)	18:47:13.16	-02:29:44.7	6.7
DF+30.31–0.28	18:47:39.03	-02:27:39.8	6.3
DF+30.36+0.11	18:46:21.16	-02:14:19.0	5.9
			7.4 ^(D)
DF+30.36–0.27	18:47:42.37	-02:24:43.2	6.9
DF+31.03+0.27 ^(B)	18:47:00.39	-01:34:10.0	4.9
			6.0
DF+36.95+0.22	18:57:59.51	+03:40:33.3	5.0
DF+51.47+0.00 ^(B)	19:26:12.74	+16:26:12.6	5.3 ^(D)

^(A) Observed in April'99 (continuum)

^(B) Observed both in April'99 and August'99

^(C) More than one value may be given in case several lines are detected on the line of sight

^(D) Distance of the tangent point is assumed

from the Massachusetts-Stony Brook Galactic Plane CO Survey (Sanders et al. 1986) and estimated as sufficiently free of emission. Finally, whenever possible, map coverages in the orthogonal direction were achieved allowing use of the PLAITS algorithm developed by Emerson et al. (1988).

Maps of $3' \times 3'$ or $4' \times 4'$ were obtained for 7 of the fields and narrow bands of $0.5' \times 3'$ for the other ones. HCO^+ and HCN $J = 1 - 0$ lines were measured in parallel with ^{13}CO and C^{18}O (HCO^+ and HCN data are not discussed here). Examples of integrated maps are given in Fig. 1 and 2. Noise levels (rms) reached are around 0.26 K (0.53 K) at 3 mm (1.3 mm) per regridded pixel and spectral resolution elements of 80 kHz. Three of the targets were observed in a second run in HC_3N and CH_3CCH (see transitions in Table 1). HC_3N maps of $1.4' \times 1.4'$ were obtained to further allow for accurate comparison of lines at different frequencies by restoring all data to a common synthetic beam. Transitions of CH_3CCH were observed in position switching, yielding a 20 mK rms level per spectral resolution element.

2.2. Continuum observations

Five clouds were mapped using the MPIFR 37-channel bolometer array centred at $\sim 1.2 \text{ mm}$ (Kreysa 1992, Kramer et al. 1998). We used the on-the-fly mode for continuum observations, consisting of dual-beam rasters with scanning velocities of $6''/\text{sec}$ or $8''/\text{sec}$. The spatial sampling interval in elevation was larger than generally used at the 30-m telescope. With a vertical offset of $24''$ (instead of $4\text{--}5''$), individual detector maps are *under-sampled* but the co-added final map is fully sampled (Teyssier & Sievers

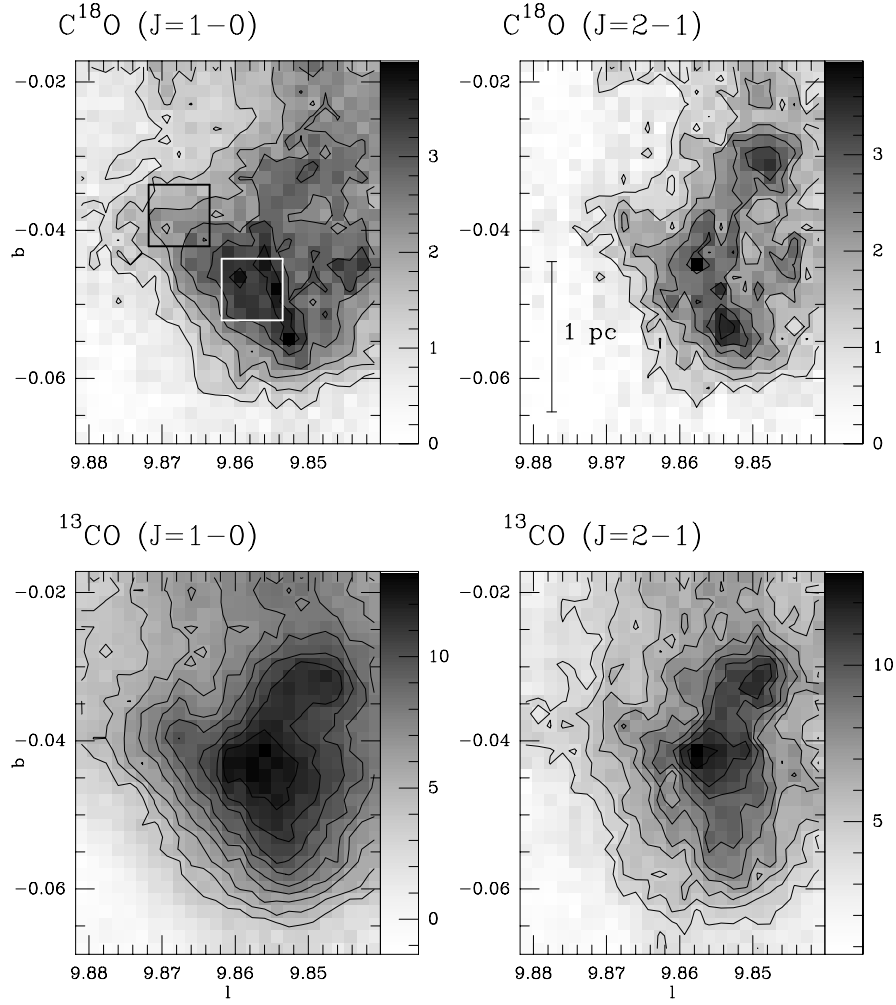


Fig. 1. Maps of CO isotopomers integrated emission for DF+09.86–0.04. Contours are 1 to 4 K km s^{−1} by steps of 0.5 for C¹⁸O transitions and 4 to 12 K km s^{−1} by steps of 1 for ¹³CO maps (T_A^{*} scale). Velocity interval is 16–20 km s^{−1}. The white box indicates the *core* position while the black one frames the *envelope* area used in the analysis.

1999). In a relatively short time (about 20 minutes) we could cover areas of 7'×6' with homogeneous observing conditions and a small field curvature when re-projecting in the equatorial frame. All maps were repeated several times at different hour angles and with different wobbler throws (46'', 56'' and 78'') in order to allow the restoration of all spatial frequencies (see Emerson et al. 1995, or Pierce-Price et al. 2001). This additional information, however, is not used by the IRAM data reduction software (NIC, Broguière et al. 1999) that we have used to derive the images presented here. A straightforward restoration algorithm (Emerson, Klein & Haslam 1979) is applied instead, followed by zero-order baseline subtraction and a systematic skynoise removal. Fig. 3 gives an example of two of these maps.

The beam size at 1.2 mm was measured to be $\sim 11''$ using Uranus. The calibration was achieved through regular on-the-fly and on-off observations on planets (Uranus and

Mars). We estimated both relative and absolute calibration to be within $\sim 10\%$. The zenith atmospheric optical depth was found to be between ~ 0.1 and ~ 0.3 , according to regular antenna tipping.

3. Observational properties

3.1. Identification of the clouds and spatial distribution

The infrared absorption features coincide remarkably with the C¹⁸O emission ridges (left and middle panels of Fig. 4), as well as with the continuum emission, although sometimes to a smaller extent (right hand panels of Fig. 4). In some of the clouds local peaks in the millimetre maps coincide with the mid-IR emission of embedded stars or stellar clusters seen by ISO. The identification of OH and CH₃OH masers (Caswell et al. 1995, see Fig. 3) associ-

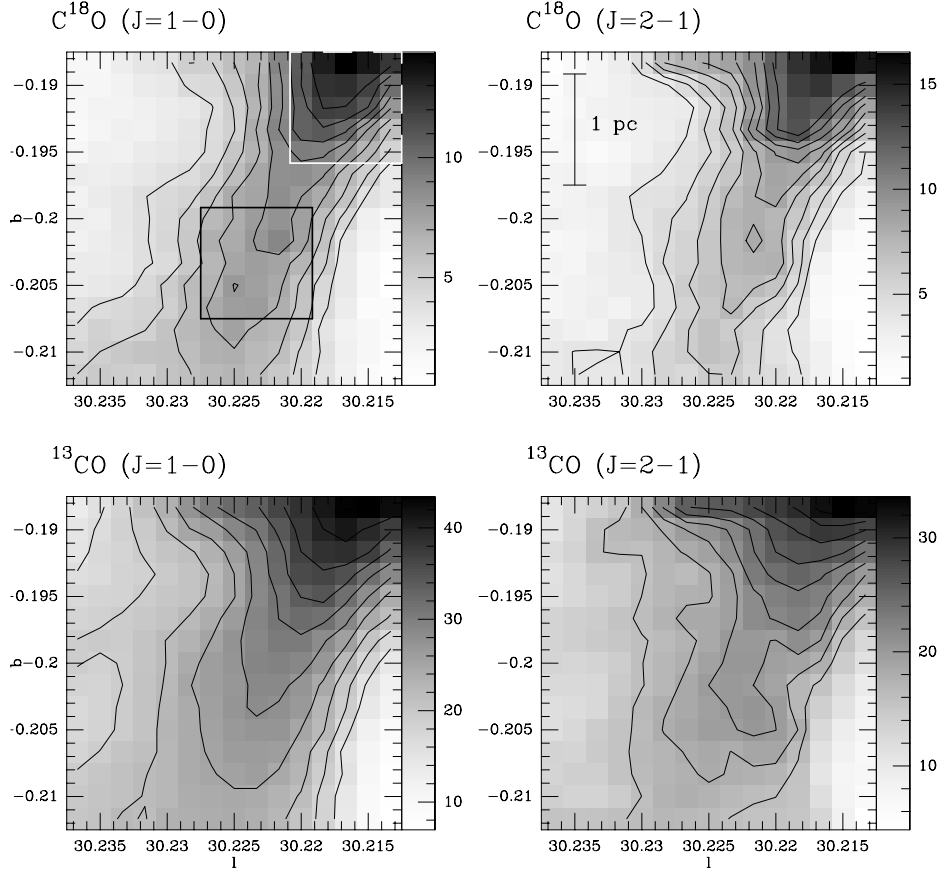


Fig. 2. Same as Fig. 1 for the central area of DF+30.23–0.20. Contours are 4 to 12 K km s^{-1} by steps of 1 for C^{18}O transitions, 16 to 35 K km s^{-1} by steps of 2 for $^{13}\text{CO}(J = 2 - 1)$ and 16 to 45 K km s^{-1} by steps of 3 for $^{13}\text{CO}(J = 1 - 0)$ (T_{A}^* scale). Velocity interval is 103–107 km s^{-1} . The black box indicates the *filament* position while the white one frames the *star edge* area.

ated with these bright sources give additional evidence that stars may have formed recently.

Fig. 3 and 4 illustrate such cases. For DF+09.86–0.04, the embedded stars appear as two small black squares indicated by arrows in the infrared data (marked with white stars in the continuum map). For DF+30.23–0.20, the stars themselves have not been mapped in CO, but are clearly seen as strong spots in continuum (white stars symbols). The dark filament turns to a bright filament in the mid-IR, while its millimetre emission is strongly reinforced around newly formed stars (Fig. 3).

Some of the clouds present several emission line components along the line of sight (e.g. DF+30.36+0.11 and DF+31.03+0.27, which are the most distant clouds of our sample). The structures associated with different velocity components present very different shapes and orientations, which sometimes need to be combined to reproduce the shape of the dark cloud. For all clouds the velocity field exhibits significant structure, as illustrated for one component of the DF+31.03+0.27 cloud by the channel maps of Fig. 5. In this object, the profiles are complex

and the gas structures seem to be connected over a wide velocity range.

Large field maps obtained with the 4-m Nanten telescope in $^{13}\text{CO}(J = 1 - 0)$ (Zagury et al., yet unpublished data) and shown on Fig. 6 for DF+09.86–0.04 and DF+30.23–0.20 indicate that the IR dark clouds are not isolated objects: they are embedded in quiescent GMC’s, most of them belonging to the cold GMC population detected earlier in CO galactic surveys (e.g. Sanders et al. 1986). This contradicts Egan et al.’s (1998) claim that the IRDCs are isolated objects.

Using the galactic rotation model of Burton et al. (1991), we are able to derive kinematic distances of these objects from the Doppler shift of the line. Assuming that the kinematic distance ambiguity is solved by the absorption bias in favour of the nearest position, we derive distances between 2.8 and 7.4 kpc (see Table 2). For all observed clouds the inferred kinematic distances are consistent with objects lying within or in front of the molecular ring.

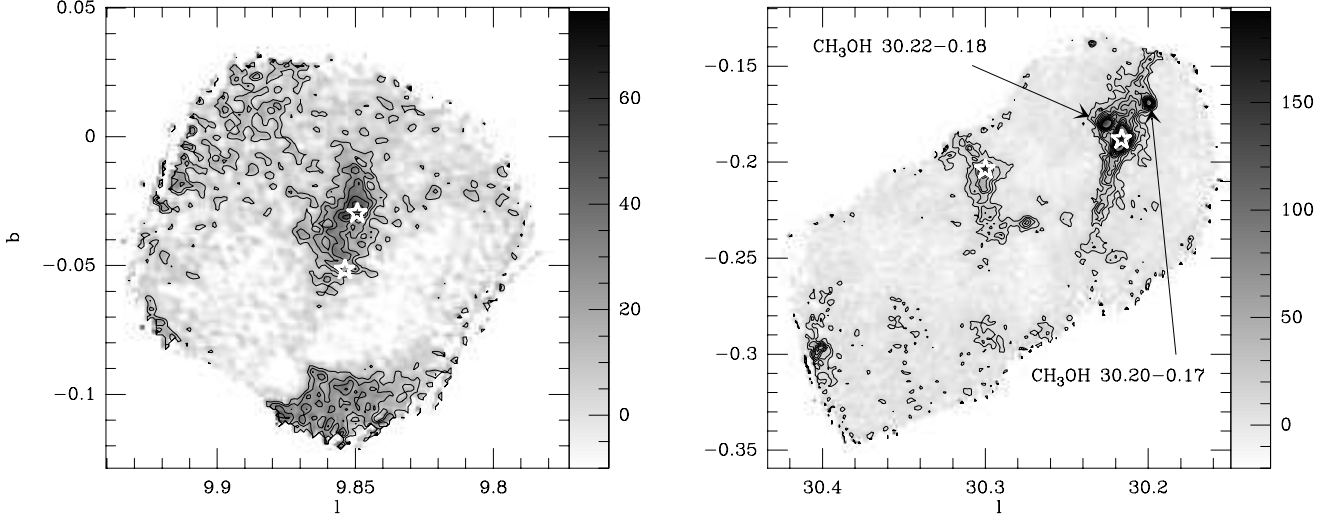


Fig. 3. Continuum maps at 1.2 mm. *Left:* DF+09.86–0.04. Contours are 10 to 60 mJy/11'' beam by steps of 10. *Right:* DF+30.23–0.20 and surroundings. Contours are 10 to 100 mJy/11'' beam by steps of 10, then 100 to 200 by steps of 50. CH₃OH masers detected in previous surveys (Caswell et al. 1995) are indicated. White star symbols indicate embedded stars identified in the mid-IR plates. Positions are in galactic coordinates.

3.2. Line intensities and velocity structure

Figs. 7 and 8 give examples of the line profiles observed in three of the clouds for so-called *core* (C¹⁸O emission peaks) and *envelope* (core periphery) areas. The lines, although often centrally peaked, rarely exhibit symmetric Gaussian profiles. In the 2 cases where embedded stars are associated with the clouds, the profiles appear as self-reversed in ¹³CO($J = 2 - 1$) and flat-topped in ¹³CO($J = 1 - 0$). DF+30.23–0.20 illustrates one of these cases (upper panel of the second column of Fig. 7). The line broadening due to a higher opacity in the star vicinity is quite significant.

The absolute line intensities are smaller than what would be expected from such massive dense clouds if extrapolated from values observed in local dark clouds (Table 3). This effect is even stronger for weaker lines like HC₃N or CH₃CCH where the lines are a factor of 5 weaker than in e.g. TMC-1 (Pratap et al. 1997). Part of this weakness may be attributed to a very low kinetic temperature or a small filling factor. But chemical effects or, most likely, depletion onto grains should be also considered. On the other hand, the lines are broader than in local dark clouds: this is not surprising given the large size and mass of the objects.

Line intensities ratios are compared in the scatter plots of Fig. 9 and 10. The ¹³CO($J = 1 - 0$) to ¹³CO($J = 2 - 1$) (noted R_{13}) and C¹⁸O($J = 1 - 0$) to C¹⁸O($J = 2 - 1$) (noted R_{18}) ratios are found to be constant on average for a given source, independent of the choice of pixels in the line centre or wings, in the cloud core or envelope. A similar result was found by e.g. Falgarone et al. (1998) for dense cores close to the Sun ($d \lesssim 150$ pc). A signifi-

Table 4. $J = 2 - 1$ to $J = 1 - 0$ ratios for C¹⁸O and ¹³CO estimated over the entire clouds.

Name	R_{18}	$R_{18}^{(A)}$	R_{13}	$R_{13}^{(A)}$
DF+04.36–0.06	0.66	0.84	0.59	0.60
DF+09.86–0.04	0.96	1.26	0.93	0.92
DF+15.05+0.09	0.62	0.82	0.72	0.78
DF+18.56–0.15	— ^(B)	— ^(B)	0.59	0.61
DF+18.79–0.03	1.02	1.18	0.66	0.70
DF+25.90–0.17	— ^(B)	0.70	0.53	0.60
DF+30.23–0.20 ^(C)	1.58	1.63	1.02	1.01
DF+30.36+0.11	1.07	1.17	0.74	0.87
“(2 nd component)”	0.90	1.24	0.94	0.79
DF+31.03+0.27	0.63	0.85	0.61	0.69
“(2 nd component)”	0.84	1.07	0.75	0.82
DF+51.47+0.00	0.70	0.78	0.60	0.63
Mean	0.90	1.05	0.72	0.75
(1- σ deviations)	± 0.28	± 0.27	± 0.15	± 0.13

^(A) Ratio of integrated intensities

^(B) Dispersion is too large

^(C) Measured between 103 and 110 km s^{−1}.

cant departure from this general behaviour is however observed in the close vicinity of the young stellar objects of DF+30.23–0.20: in the line wings the R_{13} ratio is higher than the average value obtained for the filament (right-most data points of Fig. 10). The excitation is certainly higher and the ($J = 2 - 1$) transition is optically thicker than the ($J = 1 - 0$) one, which results in a broader line and eventually in some self-absorption (Fig. 7).

Table 4 compiles the best-fit results of these ratios. The ratios between integrated intensities are also given

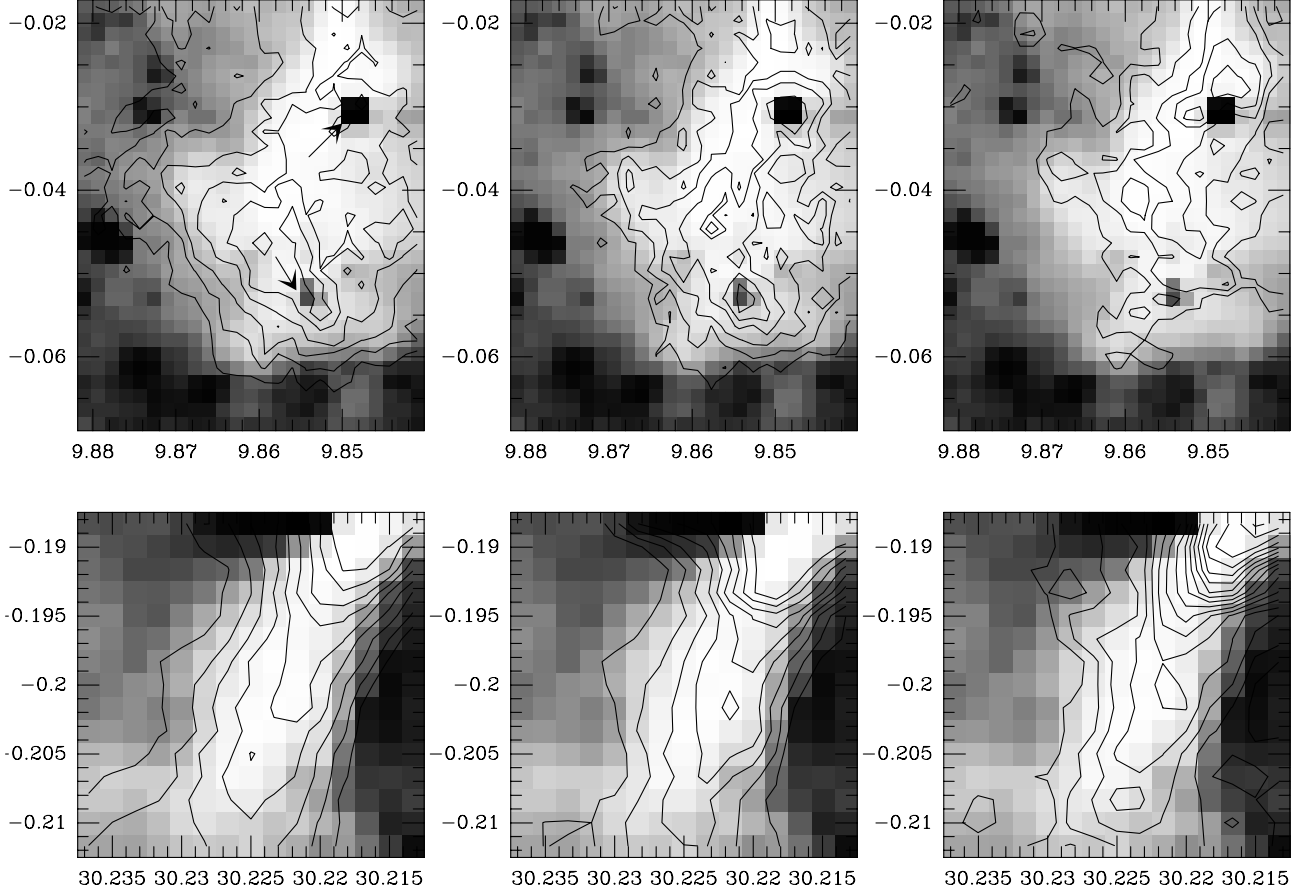


Fig. 4. **Upper panels:** *Left:* Contour map of the $\text{C}^{18}\text{O}(J=1-0)$ transition integrated emission for DF+09.86–0.04 superimposed over the corresponding ISOGAL field in the LW3 (15 μm) filter. ISOGAL data have been reversed so that absorption features appear with positive values (see text). Arrows indicate positions of embedded stars. *Middle:* same for the $\text{C}^{18}\text{O}(J=2-1)$ transition. In both cases, contours are 1 K km s^{-1} to 4 K km s^{-1} by steps of 0.5 (T_{A}^* scale), velocity interval is 16 to 20 km s^{-1} . *Right:* Contour map of 1.2 mm continuum emission for DF+09.86–0.04 superimposed over the corresponding ISOGAL field in the LW3 filter. Contours are 10 to 60 $\text{mJy}/11''$ beam by steps of 10. **Lower panels:** same as upper panels, for DF+30.23–0.20. Contours are 4 to 12 K km s^{-1} by steps of 1 for both C^{18}O maps, and 10 to 170 $\text{mJy}/11''$ beam by steps of 10 for the continuum map. Coordinates are galactic longitude and latitude.

for comparison with previous ^{12}CO studies. These results can be compared to values observed in other clouds of our Galaxy: in quiescent clouds of the solar neighbourhood, Falgarone et al. (1998) found a mean of 0.65 ± 0.15 for ^{12}CO and ^{13}CO . The C^{18}O observations reported by Kramer et al. (1999) in IC5146 lead to a mean value of 0.83 ± 0.22 . Several studies have been conducted in the Galactic plane in ^{12}CO , showing a large-scale gradient of the integrated intensity ratios: 0.75 at ~ 4 kpc from the Galactic centre, to 0.5 at 8 kpc from the Galactic centre (e.g. Sakamoto et al. 1995, who derive a mean value of 0.66 ± 0.01). A similar study conducted by Oka et al. (1998) in the Taurus and the Orion A Molecular Clouds, including star-forming sites, lead to mean values of 0.53 ± 0.01 and 0.75 ± 0.01 respectively.

Our mean values of 0.72 ± 0.16 (^{13}CO) and 0.90 ± 0.29 (C^{18}O) are higher than the values found in these published studies. Even the starless sub-sample shows rather high values: 0.67 ± 0.12 (^{13}CO) and 0.79 ± 0.22 (C^{18}O). Provided relative calibration uncertainties can be excluded, these values may be characteristic of the advanced condensation stage of IRDC's.

The comparison of ^{13}CO and C^{18}O line intensities (called R_{10} and R_{21} in Table 1 for $J=1-0$ and $J=2-1$ respectively) illustrate the differential abundances, excitation states and optical depths of the two CO isotopomers. At low intensities (yet above 5σ), these intensity ratios are consistent with the local interstellar $^{13}\text{CO}/[\text{C}^{18}\text{O}]$ ratio of about 7.3 (deduced from $^{16}\text{O}/[^{18}\text{O}] = 560$ and $^{12}\text{C}/[^{13}\text{C}] = 77$, Wilson & Rood 1994), but they depart

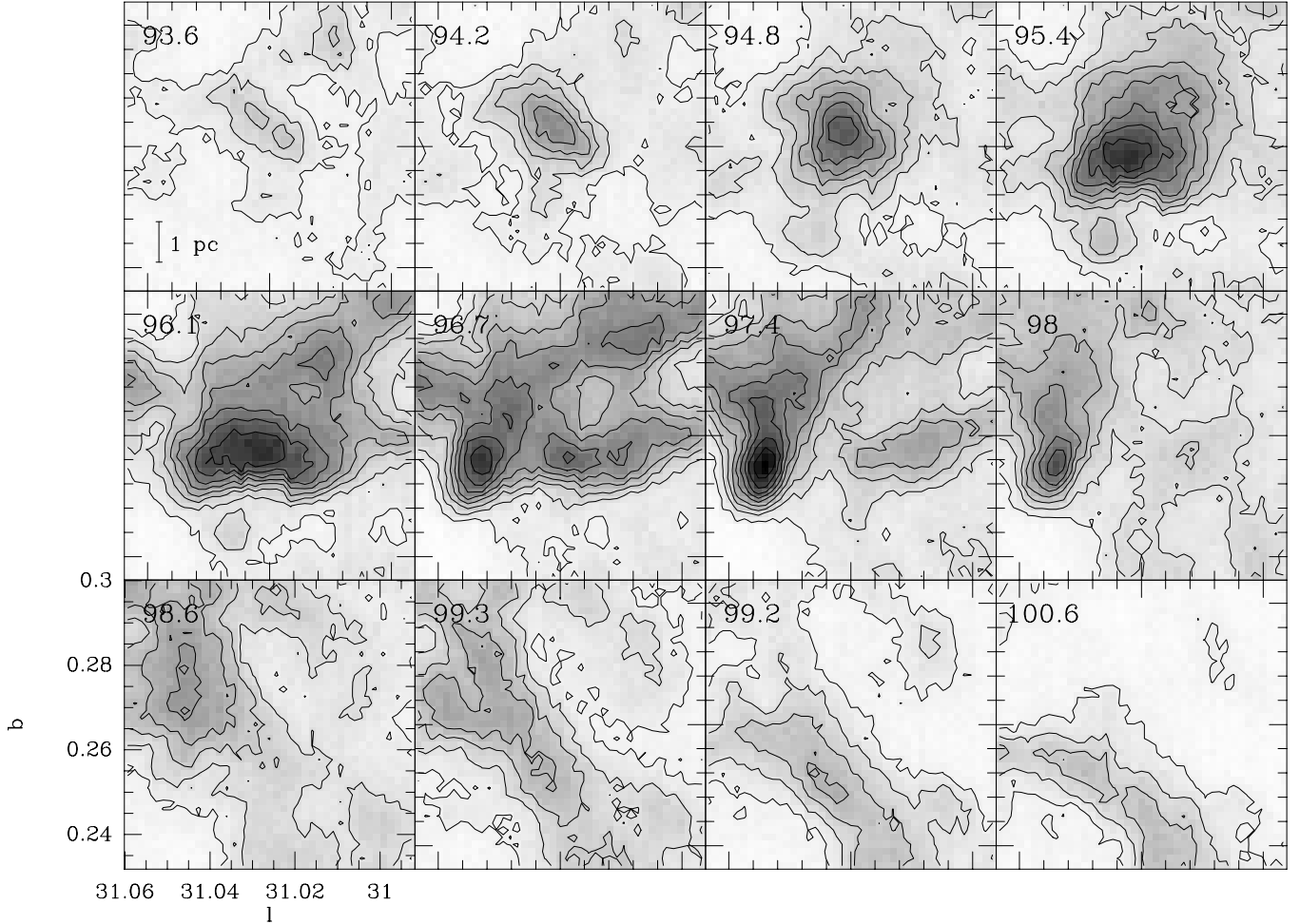


Fig. 5. $^{13}\text{CO}(J=1-0)$ channel maps of DF+31.03+0.27 averaged over 3 channels of 0.21 km s^{-1} . The central velocity in km s^{-1} is indicated on the upper left corner for each map. Contours are 0.4 to 6.7 K km s^{-1} by steps of 0.7 (T_{A}^* scale).

from this value as intensities increase. The ratios drop below 2 close to the emission peaks. These ratios are systematically larger in the envelope than in the core areas. The slow apparent saturation of the stronger line should be accounted for by detailed models.

4. Cloud properties

Preliminary results are derived from a simple analysis of the available data: spectroscopic intensities are interpreted with “LVG” calculations, which should be seen as the lowest order approximation (1-zone) to radiative transfer calculations.

4.1. Temperatures and densities from spectroscopic data

We used the spectra obtained in the $J=5-4$ and $6-5$ transitions of CH_3CCH (Fig. 8) to derive the kinetic temperatures in a subset of lines of sight. The details of this analysis will be presented in a subsequent paper (Teyssier

et al. 2001b). The temperatures inferred are in the range $8\text{--}25 \text{ K}$. The highest temperatures are representative of clouds with embedded stars (e.g. DF+30.23–0.20). These are also the only areas where significant emission is detected in the $K=2$ rotation level.

We use these temperatures to derive densities and molecular column densities from LVG simulations of HC_3N , ^{13}CO and C^{18}O . The HC_3N transitions are relatively close in energy so that the error bars are somewhat large. The densities derived are larger than 10^5 cm^{-3} in the densest parts (*cores*). Observations of lower frequency transitions are included for more accurate derivations in our subsequent paper (Teyssier et al. 2001b). The corresponding masses vary between 2×10^2 and $2 \times 10^4 M_{\odot}$. The temperatures and densities of our sample clouds are similar to the parameters reported by Carey et al. (1998) for the MSX IRDC’s.

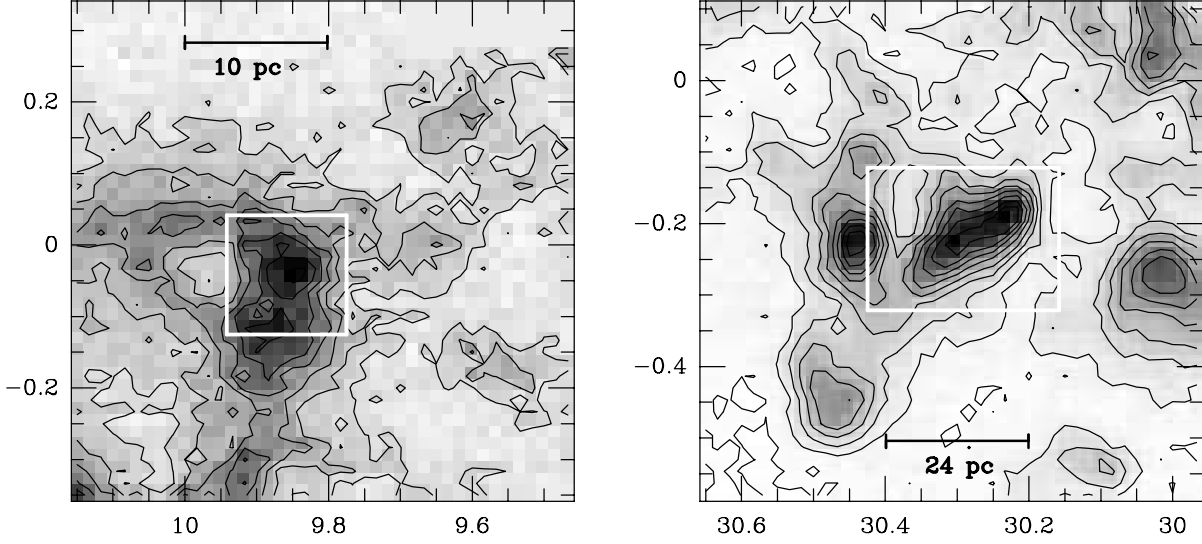


Fig. 6. Large field maps of DF+09.86–0.04 (left) and DF+30.23–0.20 (right) in the $^{13}\text{CO}(J = 1 - 0)$ transition. Beam HPBW is $2.5''$ and sampling interval is $1''$. Velocities are integrated between 16 and 20 km s^{-1} and 104 and 107 km s^{-1} respectively. The spatial connections with larger scale structures is clear. White boxes indicate the extent of the bolometer maps displayed in Fig. 3.

4.2. Column density comparison

For several of the sources we can compare independent estimates of total column densities: from mid-IR opacities, from dust 1 mm emission, from densities and size estimates, or from the column densities of tracers.

The first method consists in relating the mid-IR opacities to visible extinctions, hence total gas column density. The dust emissivity model of Draine & Lee (1984, hereafter DL84) implies:

$$A_v \simeq 65 \times \tau_{7\mu\text{m}} \quad (1)$$

The total column density along the line of sight can then be estimated using the $(N_{\text{H}+\text{H}_2}, A_v)$ relation of Bohlin et al. (1978).

The second method is based on continuum measurements of the optically thin dust at 1.2 mm and uses the relation described in Motte et al. (1998):

$$N_{\text{H}_2} = \frac{S_{1.2\text{mm}}}{\Omega_{\text{beam}} \mu m_{\text{H}} \kappa_{1.2} B_{1.2}(T_{\text{dust}})} \quad (2)$$

where S_{mm} is the 1.2 mm flux density in mJy per $11''$ beam, μ the mean molecular weight, m_{H} the mass of atomic hydrogen, $B_{1.2}(T)$ the Planck function at wavelength 1.2 mm and temperature T , and $\kappa_{1.2}$ the dust mass opacity at 1.2 mm. We adopted a value $\kappa_{1.2} = 0.003 \text{ cm}^2 \text{ g}^{-1}$, consistent with the DL84 dust model and the $(N_{\text{H}+\text{H}_2}, A_v)$ relation used in method (1). Such a value is believed to be suited to pre-stellar dense clumps and cores with a typical uncertainty of a factor of ~ 2 (see Motte et al. 1998 and ref. therein for a complete discussion). The dust temperature is assumed to be equal to the gas temperature as estimated in section 4.1.

In the third method we assume that the H_2 density derived from beam-averaged spectra is representative of the density within a sphere of projected size in the sky equal to the beam diameter. This assumption seems viable, in view of the apparent size of the core regions, but might be very uncertain, if the gas distribution is lacunar. Estimates are given both from HC_3N (method (3)) and from C^{18}O (method (3')).

Finally (method (4)), we used the $(N_{\text{H}_2}, W(\text{C}^{18}\text{O}))$ relation derived by Cernicharo & Guélin (1987, hereafter CG87) in local dark clouds. Table 5 gathers our results.

The column densities range from a few 10^{22} to at most a few 10^{23} cm^{-2} . The ratio of the estimates from methods (1) and (2) is within $\pm 15\%$ of 0.65 for all 4 cases where both estimates are available. A higher value of the emissivity at 1.2 mm (1.6 times the DL84 value) is required for matching the 2 derivations. This agrees with observations of cold condensations in the solar neighbourhood (e.g. Dupac et al. 2001). A proper account of the dust temperature distribution is in all cases requested for deriving more accurate conclusions.

Estimates from method (4) are 2 to 9 times smaller than values traced by the dust, the better agreement corresponding to the embedded star cluster of DF+30.23–0.20. Since most of the reported points have high A_v , this trend suggests possible molecular depletion onto very cold grains (see next section).

Since we considered the same core size for both cases (3) and (3'), the discrepancy between these two estimates is not surprising: it illustrates how the density derivations are limited by the different critical densities (e.g. Evans 1980). On the other hand, the column densities derived

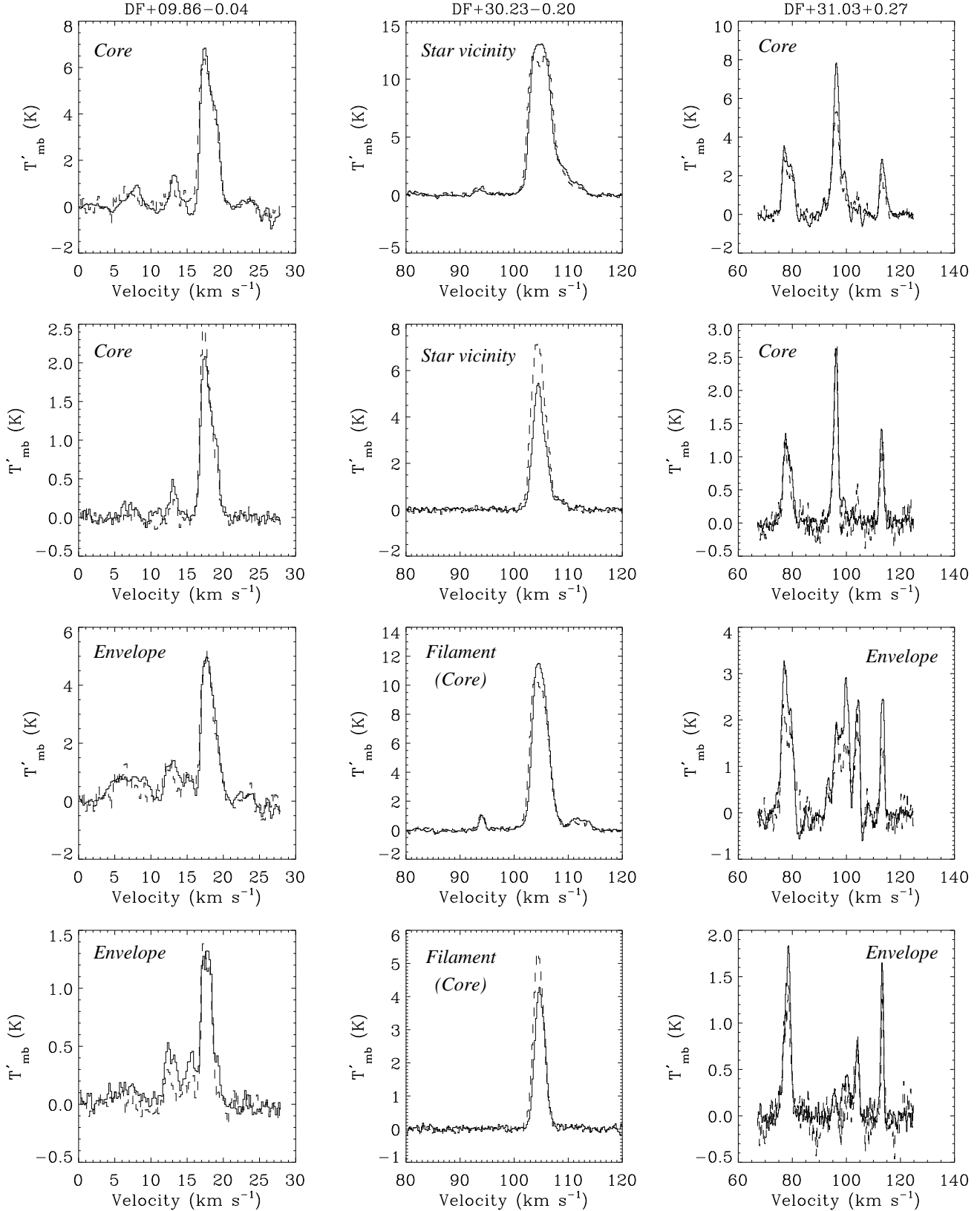


Fig. 7. Average spectra of CO isotopomers for DF+09.86-0.04, DF+30.23-0.20 and DF+31.03+0.27. First row of panels: $^{13}\text{CO}(J=1-0)$ (full lines) and $^{13}\text{CO}(J=2-1)$ (dashed lines) transitions in the core area. Second row of panels: $\text{C}^{18}\text{O}(J=1-0)$ (full lines) and $\text{C}^{18}\text{O}(J=2-1)$ (dashed lines) in the *core* (or *star vicinity*) area. Third and fourth rows of panels: same as 1st and 2nd rows for a different area of the same clouds. The spectra have been convolved to identical resolution (22'' and 0.213 km s⁻¹ channels), and averaged over 30'' boxes. Temperatures are in the T'_{mb} scale (see appendix A.1).

Table 3. CO line parameters for spectra averaged over $30'' \times 30''$ areas

Name	v_0 ^(A)	C^{18}O ^(B)		^{13}CO ^(B)		^(C)			
		$(J = 1 \rightarrow 0)$	$(J = 2 \rightarrow 1)$	$(J = 1 \rightarrow 0)$	$(J = 2 \rightarrow 1)$	R_{18}	R_{13}	R_{10}	R_{21}
DF+04.36-0.06 <i>core</i>	11.42	3.34(0.08) 1.71	2.26(0.17) 1.78	–	5.00(0.14) 1.80	0.677 (0.065)	–	–	2.21 (0.23)
<i>envelope</i>	11.37	2.10(0.08) 1.61	1.54(0.17) 1.76	–	4.05(0.14) 2.70	0.731 (0.106)	–	–	2.64 (0.38)
DF+09.86-0.04 <i>core</i> ^(E)	17.79	1.97(0.05) 2.01	2.29(0.10) 1.81	6.90(0.05) 2.52	6.22(0.10) 2.80	1.160 (0.081)	0.900 (0.020)	3.50 (0.11)	2.72 (0.16)
<i>envelope</i>	17.69	1.30(0.05) 2.12	1.39(0.10) 1.63	4.94(0.05) 2.26	4.87(0.10) 2.23	1.065 (0.118)	0.986 (0.029)	3.78 (0.19)	3.50 (0.32)
DF+15.05+0.09 <i>core</i> ^(E)	29.95	2.84(0.08) 2.05	2.16(0.13) 2.13	5.80(0.08) 2.56	4.16(0.11) 1.70	0.763 (0.066)	0.717 (0.029)	2.04 (0.09)	1.92 (0.17)
<i>envelope</i>	29.97	2.02(0.08) 2.13	1.34(0.13) 2.20	–	3.27(0.11) 1.80	0.664 (0.091)	–	–	2.44 (0.32)
DF+18.56-0.15 <i>core</i>	50.50	3.11(0.09) 1.90	1.71(0.17) 1.40	6.86(0.09) 3.25	4.54(0.16) 3.31	0.548 (0.070)	0.662 (0.032)	2.20 (0.09)	2.66 (0.36)
<i>envelope</i>	50.60	1.88(0.09) 1.53	1.16(0.17) 1.27	5.33(0.09) 2.96	3.32(0.16) 2.84	0.621 (0.120)	0.622 (0.041)	2.85 (0.19)	2.85 (0.55)
DF+30.23-0.20 <i>star vicinity</i> ^(E)	104.7	5.53(0.05) 2.52	7.62(0.13) 2.77	14.40(0.05) 3.88	13.09 ^(D) (0.13) 4.82	1.378 (0.037)	0.912 (0.012)	2.60 (0.03)	1.72 (0.05)
<i>filament</i>	104.7	4.23(0.05) 2.23	5.30(0.13) 2.28	11.90(0.05) 3.22	10.87 (0.13) 3.60	1.252 (0.047)	0.914 (0.014)	2.81 (0.05)	2.05 (0.08)
DF+30.36+0.11 <i>core</i> ^(E) (1 st component)	96.1	2.40(0.09) 3.64	3.23(0.17) 3.07	8.32(0.09) 3.42	7.53(0.17) 3.01	1.349 (0.122)	0.905 (0.030)	3.47 (0.17)	2.33 (0.18)
<i>envelope</i>	96.0	2.29(0.09) 3.14	2.28(0.17) 2.724	–	7.23(0.17) 4.09	0.997 (0.114)	–	–	3.17 (0.31)
<i>core</i> ^(E) (2 nd component)	111.0	4.00(0.09) 1.27	4.77(0.20) 1.31	–	9.47(0.18) 1.72	1.191 (0.076)	–	–	1.99 (0.12)
<i>envelope</i>	111.3	1.40(0.09) 1.57	1.94(0.20) 1.77	5.65(0.09) 2.22	4.52(0.18) 2.22	1.383 (0.230)	0.800 (0.045)	4.04 (0.32)	2.33 (0.33)
DF+31.03+0.27 <i>core</i> (1 st component)	77.8	2.12(0.05) 2.81	1.56(0.13) 2.29	4.76(0.05) 3.78	2.85(0.13) 2.98	0.736 (0.078)	0.597 (0.033)	2.25 (0.08)	1.82 (0.23)
<i>envelope</i>	78.2	1.36(0.05) 3.17	0.86(0.13) 2.86	3.65(0.05) 3.81	2.35(0.13) 3.82	0.633 (0.118)	0.645 (0.044)	2.69 (0.14)	2.73 (0.55)
<i>core</i> (2 nd component)	96.0	2.78(0.05) 2.05	2.96(0.17) 1.82	8.25(0.05) 3.42	5.38(0.15) 3.10	1.063 (0.080)	0.653 (0.022)	2.96 (0.07)	1.82 (0.15)
<i>envelope</i>	96.2	1.51(0.05) 3.71	1.56(0.17) 2.49	5.73(0.05) 4.00	4.18(0.15) 3.69	1.033 (0.146)	0.729 (0.033)	3.78 (0.16)	2.67 (0.38)
DF+51.47+0.00 <i>core</i>	54.74	2.54(0.04) 1.81	2.05(0.13) 1.80	4.82(0.04) 3.40	3.27(0.12) 2.91	0.806 (0.063)	0.678 (0.030)	1.90 (0.04)	1.60 (0.16)
<i>envelope</i>	54.38	1.73(0.04) 2.12	1.64(0.13) 2.06	4.51(0.04) 3.31	3.22(0.12) 2.82	0.948 (0.097)	0.714 (0.032)	2.61 (0.08)	1.96 (0.23)

^(A) In km s^{-1} . Centroid velocities are nearly the same for all transitions. We give here the velocity of the $\text{C}^{18}\text{O}(J = 1 - 0)$ line.

^(B) In each case, we give the peak temperature (K, in T'_{mb} scale, see appendix A.1) with its noise r.m.s. ($1\sigma_{\text{rms}}$) in brackets and the line width (km s^{-1} , $\text{FWHM}=2.35\sigma$). Temperatures correspond to data smoothed to the same spatial ($22''$) and velocity (0.213 km s^{-1}) resolution.

^(C) Brackets give the uncertainty on ratios based only on the spectra r.m.s. noise.

^(D) Extrapolated from self-reversed spectra.

^(E) Overlap with star clusters identified on the ISOGAL plates

from HC_3N ((**3**)) are generally higher than those inferred from the dust ((**1**),(**2**)). This may indicate that the actual volume filling factor is smaller than 1, the value assumed for this estimate. As in the picture proposed by Lada, Evans & Falgarone (1997) in local dense cores, this result suggests that the densest regions of the clouds are further fragmented.

4.3. Extinction

Using Eq. 1, we studied the pixel-to-pixel correlation between visual extinction and the $\text{C}^{18}\text{O}(J = 1 - 0)$ inte-

grated intensity for selected clouds. The error estimate on the mid-IR opacities is described in appendix B. Fig. 11 shows the resulting scatter diagrams. The scaling of extinction data to A_v depends on the assumed dust emissivity model. We then denote the visual extinction scale αA_v , where $\alpha = 1$ for the DL84 model. The result of bivariate fits of our data are displayed on Fig. 11. The errors resulting from the linear regression show that this best fit line is relatively well constrained, regardless of its adequacy, or not, to properly represent the data over the whole A_v range, of the intrinsic data dispersion and of the absolute calibration uncertainty.

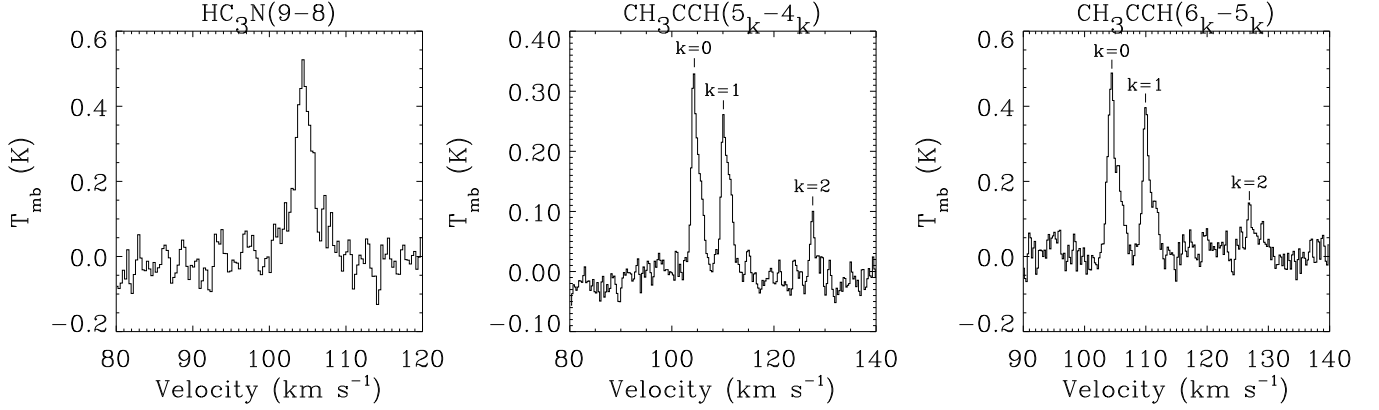


Fig. 8. Sample spectra of HC_3N , $\text{CH}_3\text{CCH}(J = 5 - 4)$ and $\text{CH}_3\text{CCH}(J = 6 - 5)$ for DF+30.23-0.20 in the star vicinity.

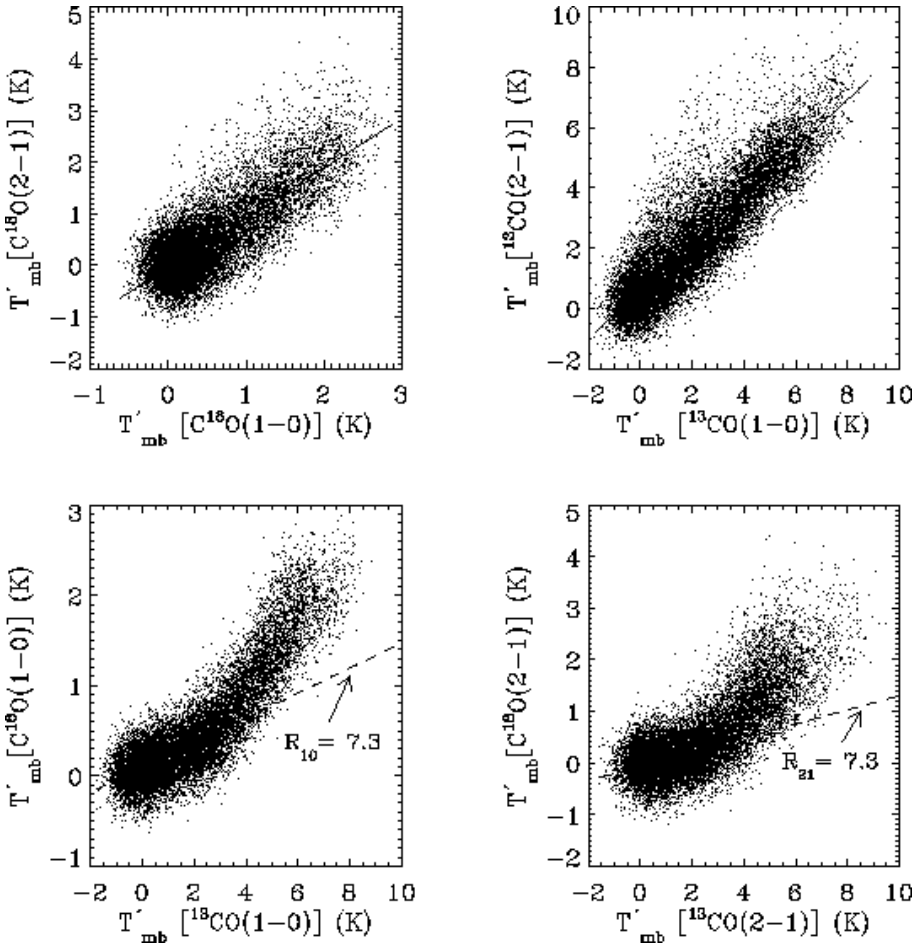


Fig. 9. Scatter plots of CO isotopomer pairs of temperatures T'_{mb} for DF+09.86-0.04 (see text). The data have been smoothed to a $22''$ spatial and 0.2 km s^{-1} spectral resolution. Velocities considered are between 16 and 20 km s^{-1} . Each 3-d pixel is represented by a dot. Best-fit results are plotted for the upper panels. Local ISM ratios are indicated by dashed-lines in the bottom diagrams.

We now compare our results to earlier studies of local dark clouds, based on star counts. In HCL2, CG87 inferred for A_v ranging from 1.5 to 6 :

$$W(\text{C}^{18}\text{O}) = 0.28 \pm 0.05 \cdot (A_v - 1.5 \pm 0.3) \text{ K km s}^{-1} \quad (3)$$

For $A_v \leq 10$, Alves et al. (1999) found in L977:

$$W(\text{C}^{18}\text{O}) = 0.18 \pm 0.01 \cdot (A_v - 1.67 \pm 0.26) \text{ K km s}^{-1} \quad (4)$$

These relations are overplotted on the graphs of Fig. 11. An important difference with the earlier studies is that

the extinction ranges probed barely overlap. The different location and nature of the sampled clouds observed with different spatial resolutions might lead to large discrepancies. The different data sets nevertheless seem compatible. Our scatter diagrams exhibit a similar break as reported by Alves et al. (1999, see also Frerking et al. 1982, Lada et al. 1994) above $A_v \sim 10$ - 15 mag. In our case, the departure from the linear fit occurs at higher A_v in the range 15 - 25 magnitudes, which is about the sensitivity limit of

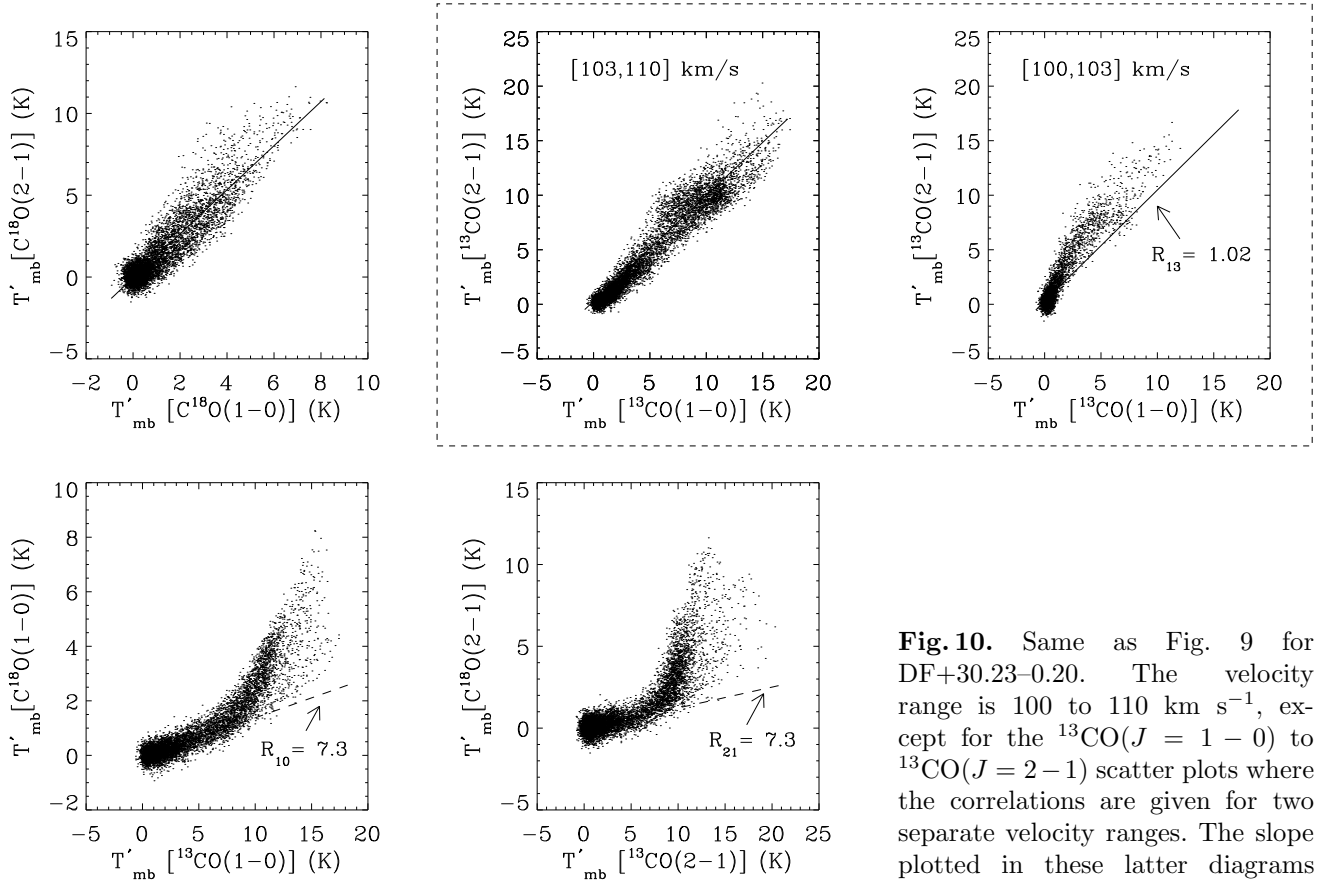


Fig. 10. Same as Fig. 9 for DF+30.23–0.20. The velocity range is 100 to 110 km s^{−1}, except for the ¹³CO(*J* = 1 − 0) to ¹³CO(*J* = 2 − 1) scatter plots where the correlations are given for two separate velocity ranges. The slope plotted in these latter diagrams corresponds to the best-fit results of the data considered between 103 and 110 km s^{−1}.

Table 5. H₂ Column densities averaged over a 20'' beam, in units of 10²² cm^{−2}

Source name	(1) N _{H₂} (mid-IR)	(2) N _{H₂} (1.2mm)	Assumed <i>T</i> _{dust} (K)	(3) N _{H₂} (HC ₃ N) (LVG+size)	(3') N _{H₂} (C ¹⁸ O) (LVG+size)	(4) N _{H₂} (C ¹⁸ O) (Cernicharo et al.)	Assumed <i>T</i> _{kin} (K)
DF+09.86–0.04 ^(A)	3.4±1.5	6.1±1.7	10	–	2.9±1.5	1.4±0.3	10
DF+09.86–0.04 ^(B)	3.1±1.4	4.8±1.7	17	–	0.6±0.1	1.1±0.2	17
DF+15.05+0.09 ^(A)	7.7±3.4	12.6±1.7	8	–	1.2±0.6	1.6±0.3	8
DF+30.23–0.20							
<i>star vicinity</i>	5.0±1.8	8.3±2.7	25	12±6	0.9±0.1	4.2±0.8	25
<i>filament</i>	8.5±3.0	11.1±1.7	8	42±28	? ^(C)	2.8±0.5	8
DF+31.03+0.27							
<i>1st component</i> ^(A)	–	11.1±1.7	10	≥10	0.75±0.15	2.0±0.4	10
<i>2nd component</i> ^(A)	–	17.7±1.7	10	12±6	3.5±1.5	2.0±0.4	10
DF+51.47–0.00 ^(A)	–	7.7±1.7	10	≥14	1.2±0.3	1.6±0.3	10

^(A) Taken at *core* position

^(B) Taken in the vicinity of the upper-right star cluster seen in Fig. 4

^(C) The density could not be constrained by the LVG model

the previous studies. It is interesting to note that the relations given in Eqs. 3 and 4 are not inconsistent with our few sample points at *A_v* below 15–20 magnitudes (e.g. DF+18.56–0.15, DF+25.90–0.17).

As for previous properties, our clouds are not all identical and their behaviour in the (*W*(C¹⁸O), *A_v*) plane may characterise different conditions:

1. *DF+15.05+0.09* and *DF+18.56–0.15*: these clouds are identified as the most opaque objects of the sample

and thus suffer most from the mismatch in the extinction ranges. Nevertheless the low extinction relations (Eqs. 3 and 4) smoothly connect to our data points and are consistent with a break at *A_v* around 15, similar to Alves et al. (1999) findings. Their conjecture that such a break is due to molecular depletion onto grains is validated by the Kramer et al.'s (1999) study based on rare CO isotopomers. The similar break found here reinforces our as-

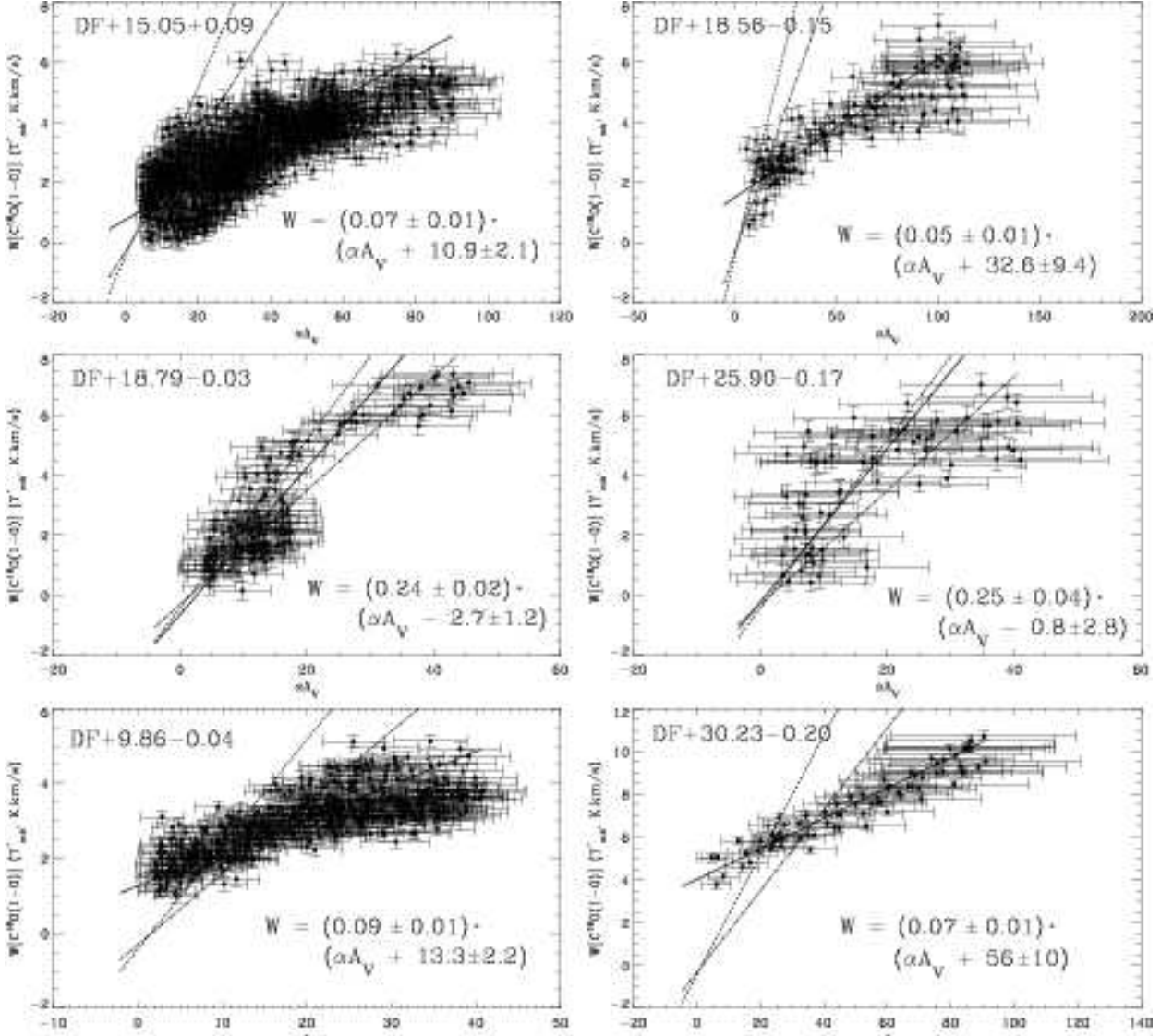


Fig. 11. Relation between the $\text{C}^{18}\text{O}(J = 1 - 0)$ integrated intensity and the visual extinction derived from mid-IR measurements in six of the clouds. α depends on the $A_V/A_{15\mu\text{m}}$ scaling; $\alpha = 1$ for DL84. IR data were smoothed to the C^{18}O beam size of $22''$. The error in the extinction measurements is calculated according to Eq. B.5 while the uncertainties on $W(\text{C}^{18}\text{O})$ correspond to the rms noise of the spectra. The solid line represents the least-square fit of the data weighted in both coordinates. The dashed (respectively dashed-dot-dot-dot) lines give the fits obtained for nearby dark clouds by Cernicharo & Guélin (1987) (resp. Alves et al. 1999) and recalled in Eq. 3 (resp. Eq 4).

sumption of significant molecular depletion inside the IR dark clouds.

2. *DF+18.79-0.03* and *DF+25.90-0.17*: these clouds present much more points in the extinction range of Eqs. 3 and 4. Although the samples are relatively scattered, we find that the data are nicely fitted by the relation of CG and Alves et al. (1999) within 10-30%, which is still consistent given the uncertainty implied by the factor α introduced above. The break position is, again, consistent with previous results and the negative intercept in agreement with Alves et al. (1999) claim that shielding is probably

not efficient enough to avoid molecular photodissociation from interstellar radiation at low visual extinctions.

3. *DF+9.86-0.04* and *DF+30.23-0.20*: these clouds exhibit a clear lack of points of weak C^{18}O emission at low visual extinctions. As mentioned in previous sections, these objects are associated with several young star clusters whose radiation probably heats the surrounding core. In *DF+30.23-0.20*, several OH and CH_3OH masers (Caswell et al. 1995) have been identified at the edge of the filament (see Fig. 3), probably tracing an even more evolved state of star-formation.

We conclude that our study extends earlier studies based on star counts in a consistent way. In particular it confirms that C^{18}O can be used as a rough column density, and thus mass, tracer in dense dark clouds, provided corrections are made to account for progressive saturation.

5. Conclusions

In this paper we presented millimetre follow-up observations of Galactic infrared dark clouds discovered in the galactic ISO survey at 7 and 15 μm . All objects are detected in ^{13}CO and C^{18}O and present remarkable spatial correlation with the mid-IR absorption data. We found that these clouds are not isolated but appear as the most condensed parts of quiescent GMC's 2 to 8 kpc away from us, some of them being associated with embedded stars or clusters observed by ISO. The clouds present a variety of shapes and line profiles indicative of supersonic flows. Velocity maps exhibit structures down to the parsec size connected to larger clouds along the line of sight.

Special attention was paid to the intensity calibration of our data and a simple approximation for extended sources seen in a main+error beam pattern was developed. Although not completely correct, it is believed to provide a better estimate of the main error beam integrated intensity than the widely used main-beam brightness temperature.

In spite of a certain diversity, some common behaviours are observed in our cloud sample. We found that the $(J = 2 - 1)$ to $(J = 1 - 0)$ ratios of ^{13}CO and C^{18}O were remarkably uniform within each object and that a significant amount of them match the values between 0.6 and 0.8 observed in local dark clouds. Higher ratios are observed in the other objects, indicative of a broader range of conditions.

A preliminary analysis of data obtained with temperature and density probes such as HC_3N and CH_3CCH shows that the clouds are mostly cold gas and dust condensations of temperatures below 10 K and densities in excess of 10^5 cm^{-3} . In those conditions, depletion onto grains is expected to strongly affect the molecular emission, but opacity effects can so far not be completely ruled out. Column densities close to 10^{23} cm^{-2} are inferred from the dust absorption and emission. These clouds are in an advanced condensation stage, and some of them already contain young stars. Similar massive dark clouds are reported by Egan et al. (1998) and Carey et al. (1998) in their MSX survey of the Galactic plane: the parameters they derive are in good agreement with ours.

The darkest condensations ($N_{\text{H}_2} \geq 10^{23} \text{ cm}^{-2}$) represent $\sim 1\%$ of the inner Galaxy surveyed with ISO. Assuming that $\lesssim 80\%$ of the population escaped detection (distance bias, confusion,...), a wild extrapolation leads to at most 10% of the dust in the inner Galaxy trapped in these cold dense cores. This is a factor ~ 50 too low to account for the hypothetical cold dust component advocated by Reach et al. (1995).

Comparison of dust mid-IR absorption and 1.2 mm emission points towards emissivities at 1.2 mm higher (factor ~ 1.6) than Draine & Lee (1984). On the other hand spectroscopic tracers indicate that the denser parts of the cold condensations are not volume filling, as earlier found in other situations (e.g. Lada et al. 1997).

We studied the relation between the integrated C^{18}O emission and the visual extinction and compared it to previous results obtained for local clouds. Our study samples higher extinctions than these former studies but we find that the correlations consistently connect in the $A_V = 15$ -25 mag range and indicate that the C^{18}O emission still is a relatively good tracer of the cloud mass at visual extinction above 15-20 magnitudes, provided corrections are made to account for radiative transfer saturation and/or depletion onto grains.

Appendix A: Observation and reduction techniques

A.1. Brightness temperature scaling

When observing extended non-uniform emission, a significant fraction of the signal is peaked by diffraction pattern components larger than the main beam. As a consequence, the widely used main beam brightness temperature scale (T_{mb} , also defined as T_{R}^* by Kutner & Ulich, 1981) overestimates the actual physical line intensity derived from the observations. Several methods have been proposed to correct from these effects (see Bensch et al. 2001a for a recent review) but most of them require additional observations to be conducted on larger scale and generally smaller telescopes.

In this work, we have used an approximation which consists of assimilating the source to a uniform disk-like emitter of brightness temperature T_{b} . If the complete beam of the instrument is known, it is possible to calculate the ratio between T_{mb} and the real T_{b} as a function of the source size. The 30-m beam is modelled according to Greve et al. (1998) as the superimposition of a main beam and three extended error beams:

$$P = \sum_{i=0,3} P_i = \sum_{i=0,3} \frac{w_i}{\Omega_i} \exp[-\ln 2 (2\theta/\theta_i)^2] d\theta \quad (\text{A.1})$$

where P_0 is the main beam beam pattern and

$$w_i = \iint_{2\pi} P_i d\Omega \quad (\text{A.2})$$

is the power fraction contained in the beam component P_i , and Ω_i its corresponding solid angle. Using the definition by Kutner & Ulich (1981), the main beam brightness temperature can be written:

$$T_{\text{mb}} = \frac{\iint_S T_{\text{b}} \star P d\Omega}{\iint_{\text{mb}} P d\Omega} \quad (\text{A.3})$$

For Gaussian beams and a disk-like uniform source of diameter θ_s and temperature T_b , Eq. A.3 finally is written:

$$T_{mb} = \frac{T_b}{\beta_0} \left[1 - \sum_{i=0,3} \beta_i \exp[-\ln 2 (\theta_s/\theta_i)^2] \right] \quad (\text{A.4})$$

with

$$\beta_i \times \iint_{2\pi} P d\Omega = w_i \quad (\text{Panis 1995}) \quad (\text{A.5})$$

Similarly, one has:

$$T_A^* = \beta_0 T_{mb}, \text{ where } \beta_0 = \frac{B_{\text{eff}}}{F_{\text{eff}}} \quad (\text{A.6})$$

is the ratio of the main beam to forward efficiency (e.g. Kramer et al. 1997). Table A.1 lists the ratios for various disk diameters. As expected, effects at 3 mm remain negligible if the source is smaller than the first error beam diameter.

To estimate the accuracy of this crude approximation, we compared it to a more accurate correction used by Falgarone et al. (1998) and Bensch et al. (2001b) on their data. We found an agreement within 10% for the brightness temperatures at 1.3 mm, where the error beam contamination is rather significant, and within 7% at 3mm, where the error beam peak-up is much smaller.

For our data, the corrections to T_{mb} amount to 5-7 % at 3 mm and to values in the range 10-70 % at 1.3 mm. Emission at a larger distance from the observed position, which is not considered here, might increase the 3 mm correction a little. For most sources the adopted correction at 1.3 mm corresponds to emission extending beyond the first error beam ($\sim 2'$ diameter). One of the greatest limitations of the method shows up for elongated sources but still the geometrical mean should represent *on average* the fraction of the source surface picked up beyond the main beam. Despite this sometimes severe limitation, we conclude that our approximate correction reasonably accounts for error beam pick-up and that the residual error on T_b is significantly smaller than the error resulting from using either T_{mb} or T_A^* .

A.2. Spurious effects in the spectral baseline

Our spectral baselines are affected by standing waves (resulting from multiple reflexions along the optical paths) and by discontinuities in the autocorrelator (AC) baseline (gain mismatch between sub-bands, also known as *platforming*). The platforming can be efficiently corrected if a wider band backend (here a filter bank) is connected in parallel. This permits us to provide an accurate 0-level to each sub-band, independent of baseline ripples that are seen equivalently in both spectrometers. A sub-band readjustment based on 0-order baselines separately estimated in each sub-band of the AC alone would indeed alter the wideband standing wave pattern and would thus bias any further correction of this additional effect.

Table A.1. Error on brightness temperature for a disk-like uniform source of diameter θ_s

θ_s (")	3 mm		1.3 mm	
	T_{mb}/T_b	T_A^*/T_b	T_{mb}/T_b	T_A^*/T_b
26.2	0.67	0.47	1.00	0.42
30	0.77	0.54	1.02	0.43
46	1.00	0.70	1.06	0.45
60	1.04	0.73	1.10	0.46
90	1.05	0.74	1.20	0.51
120	1.05	0.74	1.32	0.56
150	1.06	0.74	1.44	0.60
180	1.07	0.75	1.54	0.65
240	1.08	0.76	1.68	0.71
600	1.14	0.80	1.90	0.80
6000	1.43	1.00	2.38	1.00

Appendix B: Error calculation for mid-IR opacities

The error estimate on the opacities calculated in Paper I is based on the following formalism for the mid-IR emission:

$$I_{\text{tot}} = I_{\text{bg}} e^{-\tau} + I_{\text{fg}} \quad (\text{B.1})$$

where I_{bg} and I_{fg} are respectively the background and foreground emission w.r.t. the cloud of opacity τ . We assume that the main uncertainty on τ comes from the intrinsic fluctuations of I_{bg} and I_{fg} , of total rms amplitude ϵ , which we estimate in unobscured neighbouring regions. Using the parameter β introduced in Paper I:

$$\beta = \frac{I_{\text{bg}}}{I_{\text{tot}}} \quad (\text{B.2})$$

the fluctuations of I_{bg} and I_{fg} are written:

$$\epsilon_{\text{bg}} = \sqrt{\beta} \epsilon, \text{ and } \epsilon_{\text{fg}} = \sqrt{1 - \beta} e^{-\tau} \epsilon \quad (\text{B.3})$$

Assuming that these contributions are uncorrelated, this leads to:

$$\delta\tau^2 \simeq \left(\frac{\epsilon_{\text{bg}}}{I_{\text{bg}}} \right)^2 + \left(\frac{\epsilon_{\text{fg}}}{I_{\text{bg}}} \right)^2 \quad (\text{B.4})$$

$$\simeq \left(\frac{\epsilon}{I_{\text{tot}}} \right)^2 \left[\frac{1}{\beta} + \frac{1 - \beta}{\beta^2} e^{-\tau} \right] (e^\tau)^2 \quad (\text{B.5})$$

This approach tends to favour the lowest extinction points of our samples but takes into account the fact that errors on nearby objects ($\beta \lesssim 1$) are smaller.

Acknowledgements. We thank the anonymous referee for constructive comments and suggestions that improved the paper. We also would like to thank Christoph Nieten for providing us with a modified version of the FLYPLAIT program for data reduced with the GILDAS software. D. Teyssier is very grateful to the IRAM 30-m staff for his help and assistance during his period there. We also acknowledge P. Schilke for providing his LVG code. We would like to thank J.F. Panis for the very useful discussions on temperature scaling and for making the IRAM key-project raw database available to us. F. Zagury of Nagoya University made the observations at the 4-m Nanten telescope.

References

- Alves J., Lada C.J., Lada E.A., 1999, *ApJ* 515, 265
- Bensch F., Stutzki J., Heithausen A., et al. 2001a, *A&A* 365, 285
- Bensch F., Panis J.-F., Stutzki J., Heithausen A., et al. 2001b, *A&A* 365, 275
- Bohlin R.C., Savage B.D., Drake J.F., 1978, *ApJ*, 224, 132
- Broguière D., Neri R., Sievers A., 1999, *NIC Bolometer Users Guide*
- Burton W.B., Elmegreen B.G., Genzel R., In: “The Galactic Interstellar Medium”, Saas-Fee Advanced Course 21, lectures notes 1991, Swiss-Society for Astrophysics and Astronomy.
- Carey S.J., Clark F.O., Egan M.P., Price S.D., Shipman R.F. et al., 1998, *ApJ* 508, 721
- Carey S.J., Feldman P.A., Redman R.O., Egan M.P., MacLeod J.M. et al., 2000, *ApJ* 542, L157
- Caswell J.L., Vaile R.A., Ellingsen S.P., Norris R.P., 1995, *MNRAS*, 274, 1126
- Cernicharo J., Guélin M., 1987, *A&A* 176, 299
- Draine J.T., Lee H.M., 1984, *ApJ* 285, 89
- Dupac X., Giard M., Bernard J.-P., Lamarre J.-M. et al., 2001, *ApJ* 553, 604
- Egan M.P., Shipman R.F., Price S.D., Carey S.J., Clark F.O. et al., 1998, *ApJ* 494, L199
- Emerson D.T., Klein U., Haslam C.G.T., 1979, *A&A*, 76, 92 (EKH)
- Emerson D.T., Gräve R., 1988, *A&A*, 190, 353
- Emerson D.T., Payne J.M., 1995, *Multi-Feed Systems for Radio-Telescopes*, PASP, vol. 75, p. 332
- Evans N.J., II, 1980, in *IAU Symposium 87, Interstellar Molecules*, ed. B.H. Andrew (Dordrecht: Reidel)
- Falgarone E., Panis J.-F., Heithausen A., Pérault M., Stutzki J. et al., 1998, *A&A*, 331, 669
- Frerking M.A., Langer W.D., Wilson R.W., 1982, *ApJ*, 262, 590
- Greve A., Kramer C., Wild W., 1998, *A&AS*, 133, 271
- Hennebelle P., Pérault M., Teyssier D., Ganesh S., 2001, *A&A* 365, 598 (Paper I)
- Kramer C., 1997, *Calibration of spectral line data at the IRAM 30-m telescope*, IRAM internal report
- Kramer C., Thum C., Sievers A., 1998, *A Short Guide to Observations with the MPIfR Multi-channel Bolometer at the 30-m IRAM Radiotelescope*, IRAM internal report
- Kramer C., Alves J., Lada C.J., Lada E.A., Sievers A. et al., 1999, *A&A*, 342, 257
- Kreysa E., 1992, In: ESA, Proceedings of an ESA Symposium on Photon Detectors for Space Instrumentation p.207-210 (SEE N94-15025 03-19)
- Kutner M.L., Ulich B.L., 1981, *ApJ*, 250, 341
- Lada C.J., Lada E.A., Clemens D.P., Bally J., 1994, *ApJ*, 429, 694L
- Lada E.A., Evans N.J., II, Falgarone E. 1997, *ApJ*, 488, 286
- Mauersberger R., Guélin M., Martín-Pintado J., Thum C., Cernicharo J. et al., 1989, *A&AS*, 79, 217
- Motte F., Andre P., Neri R. 1998, *A&A*, 336, 150
- Oka T., Hasegawa T., Hayashi M., Handa T. et al., 1998, *ApJ* 493, 730
- Omont A., Ganesh S., Alard C., Blommaert J.A., Caillaud B. et al., 1999, *A&A* 348, 755
- Panis J.-F. 1995, PhD dissertation
- Pérault M., Omont A., Simon G., Seguin P., Ojha D. et al., 1996, *A&A* 315, L165
- Penzias A.A., Burrus C.A., 1973, *ARA&A* 11, 51
- Pierce-Price D., Richer J.S., Greaves J.S., Holland W.S., Jenness T. et al., 2001, *ApJ* 545, L121
- Pratap P., Dickens J.E., Snell R.L., Miralles M.P., Bergin E.A. et al., 1997, *ApJ* 486, 862
- Reach W.T., Dwek E., Fixsen D.J., Hewagama T., Mather J.C. et al., 1995, *ApJ* 451, 188
- Sanders D.B., Clemens D.P., Scoville N.Z., Solomon P.M., 1986, *ApJS* 60, 1S
- Sakamoto S., Hasegawa T., Hayashi M., Handa T. et al., 1995, *ApJS* 100, 125
- Teyssier D., Sievers A., 1999, *A Fast-Mapping Method for Bolometer Array Observations at the IRAM 30-m Telescope*, IRAM Technical report
- Teyssier D., Pérault M., Hennebelle P., 2001b, in preparation
- Ungerechts H., Brunswig W., Kramer C., Lucas R., Paubert G. et al., 1999, *IRAM 30-m Telescope Spectral Line On-The-Fly Mapping*, IRAM report
- Wilson T.L., Rood R., 1994, *ARA&A*, 32, 191